



Research article

Low-profile 700 MHz conformal omni-directional antenna for commercial wireless and safety communication wearable applications

Ravi Kumar Thella, Jayendra Kumar*

School of Electronics Engineering, VIT-AP University, Inavolu, Andhra Pradesh-522 237, India

ARTICLE INFO

Keywords:

Compact antenna
Conformal antenna
Meander line antenna
Polyimide substrate
Wireless and safety communication

ABSTRACT

The 700 MHz public safety spectrum is released for commercial wireless and safety communication wearable applications (CWSC-WA). However, the 700 MHz band need a larger aperture for an efficient radiation due to a larger wavelength. In this paper, we have systematically developed a novel miniature omnidirectional 700 MHz antenna for the CWSC-WA. Over 40% miniaturization is realized by truncating the ground plane and a meander line inspired radiator compared to a conventional rectangular patch antenna. The truncation of the ground plane also yields a perfect omnidirectional radiation pattern desired for the CWSCA. Considering current and future demands of wearable electronics and virtual reality, the antenna is made on a flexible substrate and conformity analysis is also performed. The prototype of the antenna is developed and simulated results are verified in planar as well as conformal configurations.

1. Introduction

The Federal Communications Commission (FCC) has revised regulations to establish a nationwide public safety broadband network in the 700 MHz band (698-806 MHz) for local and state public safety entities [3]. Achieving impedance matching beneath the patch requires a feeding network due to diverse electric field distributions [4]. There's a demand for low-profile ultra-wideband (UWB) antennas for both civil and military applications, which poses challenges in maintaining wideband performance at low frequencies. Achieving this for omnidirectional monopole antennas while ensuring high gain and reliable unidirectional patterns for airborne platforms has been explored by various designers [1]. The low-profile decoupling structure, derived from patch antenna array phase shift concepts, is particularly relevant for MIMO systems, offering integration ease and performance versatility. A novel decoupling structure that's low-profile and compact is needed [2]. A conformal dual-band antenna with a metamaterial structure (MS) fabricated on a slim, flexible polyimide substrate is proposed for effective communication in the WBAN system. Placing the MS between the antenna and the forearm enhances gain and radiation efficiency [5]. A cost-effective dipole antenna on a flexible Kapton substrate for a 2.45 GHz RFID dosimeter tag is developed. The antenna employs artificial magnetic conductor (AMC) unit cells to maintain consistent gains under various conditions, even on a lossy blood bag [6]. In wearable technology, a bracelet-shaped UHF RFID antenna is introduced, tested on the human body, and compared with a 3-D-printed version. The flexible meandering

* Corresponding author.

E-mail address: jayendra854330@gmail.com (J. Kumar).

<https://doi.org/10.1016/j.heliyon.2024.e26292>

Received 30 August 2023; Received in revised form 3 February 2024; Accepted 9 February 2024

Available online 14 February 2024

2405-8440/Â© 2024 The Authors. Published by Elsevier Ltd. This is an open access article under the CC BY-NC-ND license (<http://creativecommons.org/licenses/by-nc-nd/4.0/>).

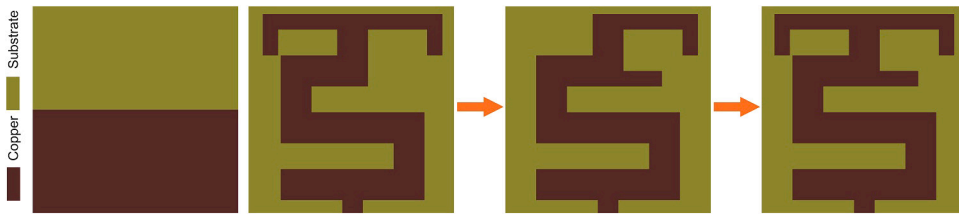


Fig. 1. Design flow of the proposed antenna (a) SA antenna (b) RHS antenna configurations (c) Proposed antenna.

patch design utilizes the substrate's properties, while the 3-D-printed PLA version employs a PIFA-inspired shape, both thoroughly validated [7].

In [8], an efficient approach is introduced for designing a dual-band dual-mode (DBDM) patch antenna, offering a flexible frequency ratio, a wide range of frequencies, and a compact structure. The patch's operating frequency is adjusted using symmetrically positioned shorting pins at the center. This adaptable design holds promise for integration into modern communication systems. In [9], a flexible, electrically small antenna with electric near-field resonant parasitic (NFRP) filtering capabilities is presented. The antenna maintains performance across various bending scenarios, crucial for space-constrained wireless communication systems dealing with complex interference challenges. A novel amplitude equalizing spoof surface plasmon polaritons (AESSPPs) filter integrated onto a flexible substrate is discussed in [10]. This filter achieves amplitude equalization and interference filtering, relocating gain compensation from complex algorithms to the microwave front end. The equalizing thin layer dissipates energy at varying frequencies, with independently adjustable equalization and bandwidth, combining flexibility, equalization, and filtering functions seamlessly. Omnidirectional antennas distribute radio wave power uniformly in all directions on a plane, forming a "doughnut-shaped" radiation pattern. They provide complete 360° coverage, crucial for wireless communication systems. A low-drag saber-like antenna serves polarization diversity and onboard omnidirectional coverage [11]. A compact cavity antenna achieves horizontally polarized omnidirectional radiation via a miniaturized design with capacitive substrate-integrated impedance surface (SIIS) for tunable resonance frequencies [12]. A scalable dual-polarized antenna uses a hybrid structure for azimuthal plane omnidirectional radiation, vital for WLAN routers [13]. On metallic surfaces, vertically polarized omnidirectional radiation occurs in tag antennas. Such tags are vital for spatial coverage applications like supermarket management and vehicular access control [14]. Conformal antennas are common in military and civilian contexts, adapting to cylindrical, elliptical, spherical, or conical shapes. A multi-layered metamaterial (MTM) antenna for WBAN communication suppresses SAR, addressing challenges from conformal fit to the human body [15]. Conformal SIW antennas in standing-wave and leaky-wave modes offer focal height control and efficient signal propagation [16]. Clothing with spoof surface plasmonic (SSP) devices enhances signal propagation around the body [17]. Recent research focuses on constant-curvature surfaces for conformal antennas, simplifying design and eliminating radomes, while non-constant curvature surfaces pose challenges [18]. Wireless capsule endoscopy transforms GI diagnostics by eliminating traditional wired endoscopy's anxieties [19]. Conformal leaky-wave antennas conform to curved surfaces, benefiting aerospace, wearable, and mobile devices [20].

In this work, we have introduced an innovative and compact narrowband antenna design, inspired by the meander line concept, optimized specifically for commercial wireless and safety communication wearable applications. The selection of narrowband antennas for wearables is driven by their ability to provide significant advantages, including improved space utilization, reduced interference susceptibility, enhanced battery life, extended communication range, adherence to regulatory requirements, and minimized interference between neighboring devices. Our antenna design achieves miniaturization while maintaining an omnidirectional radiation pattern through the strategic utilization of a partial ground plane. The operational frequency band is tuned through a series of precise radiator shaping iterations. Our antenna patch draws inspiration from modified meander line structures, resulting in a remarkably sharp and narrow resonant band centered at 700 MHz. Compared to conventional rectangular patch antennas built on the same substrate, our antenna achieves a substantial size reduction of over 40%. Furthermore, it exhibits a near-perfect omnidirectional radiation pattern and a reasonable gain, striking a balanced compromise between effective radiation and specific absorption rate (SAR). We have successfully fabricated a prototype of our antenna and conducted comprehensive performance tests in both planar and conformal configurations, with results confirming its excellent performance and suitability for wearable applications.

2. Antenna design

The design flow of the proposed antenna is shown in Fig. 1 and the dimensions of the final design are presented in Fig. 2, respectively. Figs. 1a, 1b and 1c represents SA antenna, RHS antenna configurations and the Proposed antenna, respectively. A meander line or S-shaped radiators are well-known radiators to achieve miniaturization. It has been utilized for miniaturization in several designs for decades [21–23]. However, it is challenging to optimize the size and shape of each connecting branch to obtain the desired radiation performance and impedance matching for these narrowband structures. In this work, we propose an optimized miniature and novel antenna structure for the commercial wireless and safety communication wearable applications.

The architecture of the proposed antenna and the Scattering parameters (ant1, ant2, and ant3) are illustrated in Fig. 1. The antenna structure comprises a radiating patch with a partial ground layer and a dielectric substrate. The design utilizes a 50 Ω edge feeding line. To mitigate mutual coupling and reduce back lobe radiation, a defective partial ground is incorporated as the base layer, effectively diminishing surface wave diffraction from the ground plane's edges. The chosen dielectric substrate is Polyimide, with a dielectric constant (ϵ_r) of 3.5, a loss tangent ($\tan \delta$) of 0.008, and a thickness of 0.125 mm. Polyimide is favored due to its

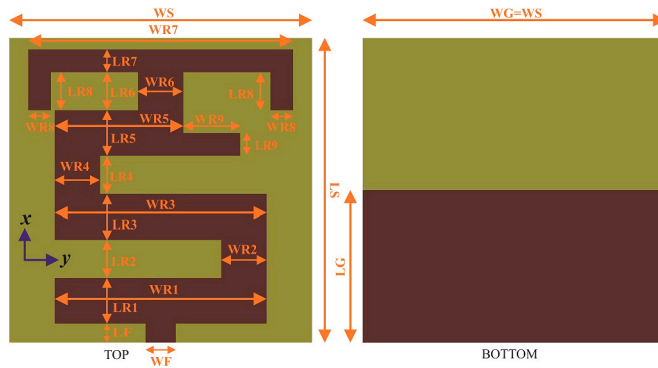


Fig. 2. Layout of the Flexible omni-directional antenna.

Table 1
Optimized values of the proposed antenna (Unit: mm).

parameter	value										
LR1	12	LR3	12	LR5	12	LR7	06	LR9	06	LG	40
WR1	56	WR3	56	WR5	34	WR7	70	WR9	15	WG	80
LR2	10	LR4	10	LR6	10	LR8	10	LF	05	LS	80
WR2	12	WR4	12	WR6	12	WR8	06	WF	08	WS	80

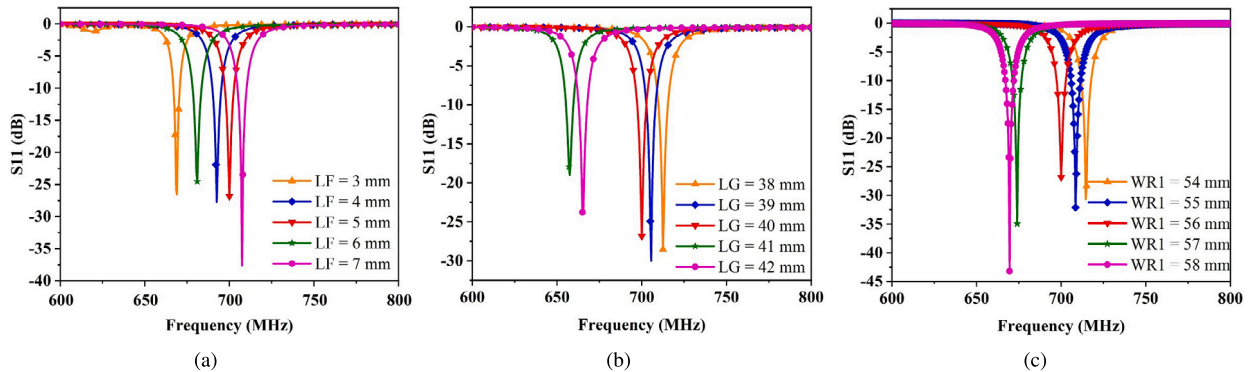


Fig. 3. Parametric analysis of S-parameters for the proposed antenna (a) LF, (b) LG, (c) WR1.

favorable physical, chemical, and electrical properties. The flexible omni-directional antenna comprises a partial ground plane ($40 \times 80 \text{ mm}^2$), a square Polyimide substrate ($80 \times 80 \times 0.125 \text{ mm}^3$), and the feeding network ($0.125 \times 8 \text{ mm}^2$). This design facilitates enhanced efficiency, reduced ground effects, and reasonably high reactive impedance across the frequency range. Fig. 1 displays the antenna’s design flow, all tuned around the same resonant frequency range of 697.30 to 702.71 MHz, achieving a stable resonance at 700 MHz. Optimization of the ground plane and feed line configuration results in improved impedance matching. Fig. 2 depicts the layout and dimensions of the proposed antenna. The final measurements of the flexible omni-directional antenna are provided in Table 1, all in millimeters.

3. Result analysis

Fig. 3(a) illustrates the variation in feed length (LF) from 3 mm to 7 mm in increments of 1 mm, accompanied by an operating frequency range spanning 669.00 to 707.50 MHz. Notably, exceptional impedance matching is maintained ($S_{11} < -10$) throughout this range. The LF progression reveals an upward trend from 3 mm to 5 mm, resulting in an increase in operating frequency. Conversely, a dip in operating frequency occurs at an LF of 6 mm, followed by an upswing at an LF of 7 mm. It’s worth emphasizing that LF serves as the frequency tuning parameter in this design. Consequently, the proposed antenna functions effectively within a tightly constrained frequency band of 697.30 to 702.71 MHz. The desired operating frequency of 700 MHz aligns with an LF of 5 mm. In Fig. 3(b), we observe the shift in ground length (LG) within a range of 38 mm to 42 mm, incremented by 1 mm steps. Simultaneously, the operating frequency spans from 657.50 to 712.50 MHz, maintaining excellent impedance matching ($S_{11} < -10$). During this process, as LG increases from 38 mm to 41 mm, the operating frequency experiences a decrease. However, at an LG of 42 mm, a minor increase in operating frequency is discernible compared to an LG of 41 mm. Notably, LG serves as the frequency tuning parameter for this design. As a result, the proposed antenna operates within a constrained frequency range of 697.30 to 702.71 MHz,

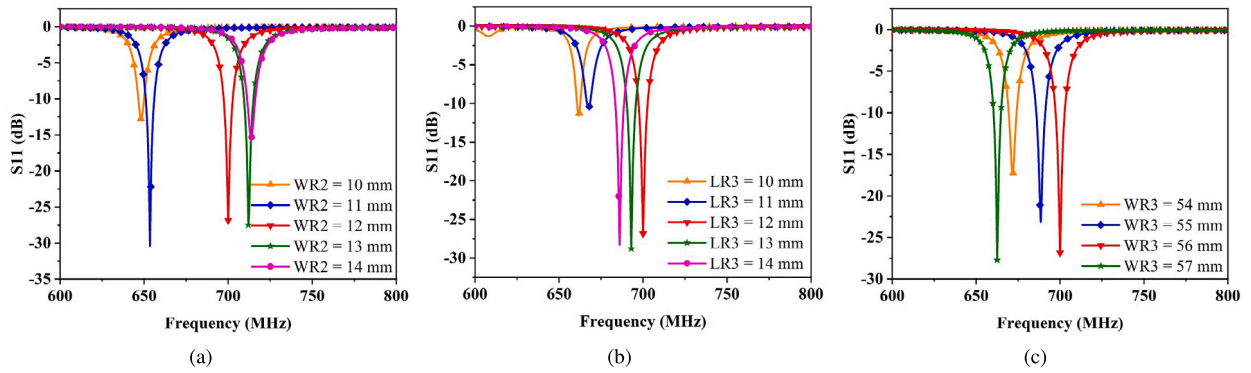


Fig. 4. Parametric analysis of S-parameters for the proposed antenna (a) WR2, (b) LR3, (c) WR3.

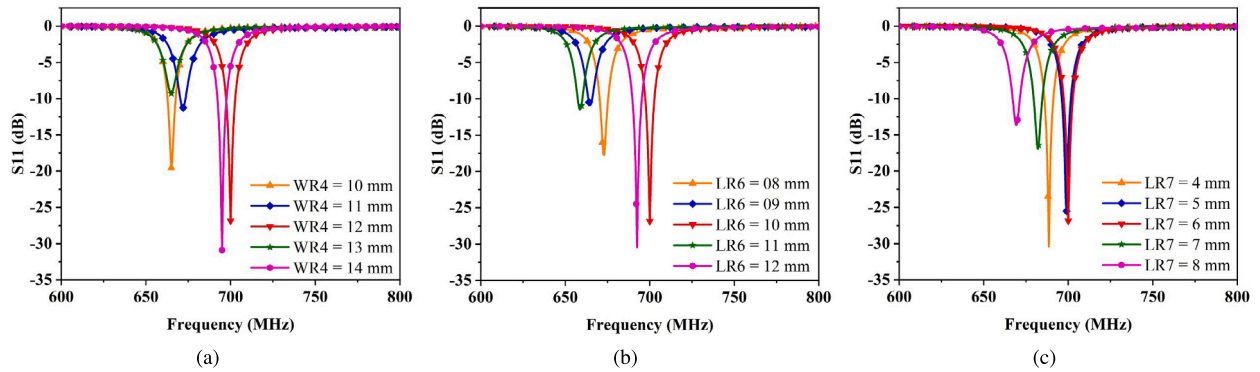


Fig. 5. Parametric analysis of S-parameters for the proposed antenna (a) WR4, (b) LR6, (c) LR7.

with an optimal operating frequency of 700 MHz corresponding to an LG of 40 mm. Moving on to Fig. 3(c), the antenna's width of rectangle1 (WR1) ranges from 54 mm to 58 mm, stepping up by 1 mm increments. Meanwhile, the operating frequency varies from 669.50 to 714.50 MHz, maintaining outstanding impedance matching. As WR1 steadily increases, a consistent downtrend in operating frequency is observed. Clearly, WR1 stands as the frequency tuning parameter governing this design. Thus, the proposed antenna efficiently operates within the confined frequency band of 697.30 to 702.71 MHz, achieving the target operating frequency of 700 MHz at a WR1 of 56 mm.

In Fig. 4(a), the width of rectangle2 (WR2) spans a range of 10 mm to 14 mm, progressing in 1 mm increments. Concurrently, the operating frequency varies between 648.50 and 714.00 MHz, showcasing exceptional impedance matching ($S_{11} < -10$ dB). As WR2 undergoes continuous expansion, the operating frequency exhibits a corresponding continuous increase. This underscores the significance of WR2 as the pivotal frequency tuning parameter for this design. Consequently, the proposed antenna operates within a slender frequency band of 697.30 to 702.71 MHz, achieving the targeted operating frequency of 700 MHz at a WR2 of 12 mm. Moving to Fig. 4(b), we examine the length of rectangle3 (LR3) ranging from 10 mm to 14 mm, incremented in 1 mm steps. Simultaneously, the operating frequency shifts between 661.50 and 700.00 MHz, maintaining excellent impedance matching ($S_{11} < -10$ dB). Notably, up to an LR3 of 12 mm, an increase in LR3 corresponds to an increase in operating frequency; however, this trend reverses after reaching 12 mm, resulting in a decrease in operating frequency. Here, LR3 emerges as the frequency tuning parameter guiding this design. Consequently, the Optimal Dual-Parametric Antenna (ODPA) fine-tunes the desired operating frequency of 700 MHz when LR3 is set to 12 mm. Once again, the proposed antenna efficiently operates within the confined frequency range of 697.30 to 702.71 MHz. Finally, in Fig. 4(c), the proposed antenna features the width of rectangle3 (WR3) spanning from 54 mm to 57 mm, with increments of 1 mm. The operating frequency ranges from 662.50 to 700.00 MHz, maintaining superb impedance matching ($S_{11} < -10$ dB). As WR3 undergoes consistent augmentation, the operating frequency exhibits a continuous increase, with the exception being when WR3 reaches 57 mm, leading to a decrease in operating frequency. WR3's role as the frequency tuning parameter is evident in its impact on the design. Consequently, the proposed antenna functions adeptly within a constrained frequency range of 697.30 to 702.71 MHz, achieving the target operating frequency of 700 MHz when WR3 is set at 56 mm.

Fig. 5(a) shows the results for the antenna's width of rectangle4 (WR4) spans 10 to 14 mm in 1 mm increments, while the operating frequency ranges from 665.00 to 700.00 MHz with exceptional impedance matching ($S_{11} < -10$ dB). WR4's continuous increase corresponds to a continuous rise in the operating frequency, except at 13 mm and 14 mm, where a decrease is observed. WR4 is the crucial frequency tuning parameter in this design. The proposed antenna operates within a confined frequency band of 697.30 to 702.71 MHz, achieving the desired 700 MHz operating frequency at WR4 of 12 mm. Fig. 5(b) shows the results for the length of rectangle 6 (LR6) ranges from 8 mm to 12 mm with 1 mm increments. Simultaneously, the operating frequency ranges

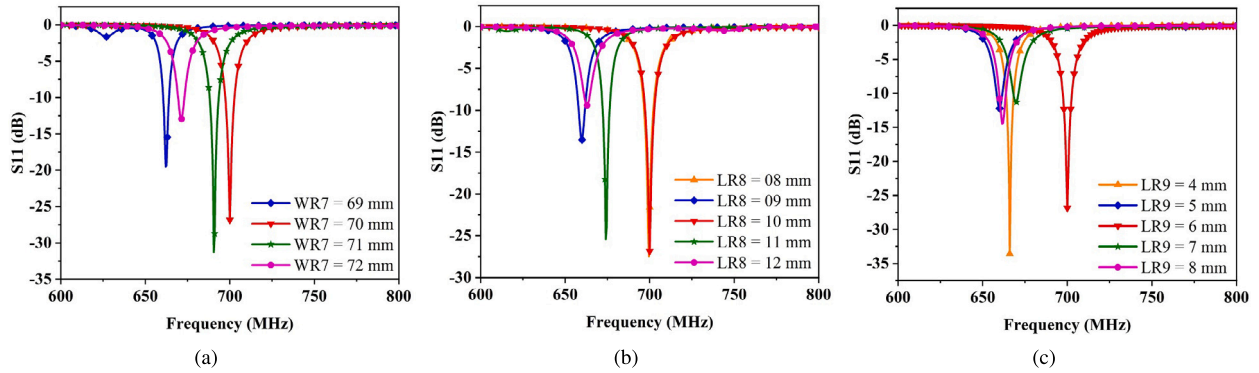


Fig. 6. Parametric analysis of S-parameters for the proposed antenna (a) WR7, (b) LR8, (c) LR9.

from 659.00 to 700.00 MHz with excellent impedance matching ($S_{11} < -10$). LR6 acts as the frequency tuning parameter, leading the proposed antenna to function within a constrained frequency range of 697.30 to 702.71 MHz. The antenna's optimal 700 MHz operating frequency is obtained when LR6 is set to 10 mm. Fig. 5(c) shows the results for the length of rectangle7 (LR7) ranges from 4 mm to 8 mm in 1 mm increments. The operating frequency varies from 669.00 to 700.00 MHz with excellent impedance matching ($S_{11} < -10$). A notable trend emerges: when LR7 increases from 4 to 6 mm, the operating frequency rises, yet an increase from 7 to 8 mm leads to a frequency decrease. LR7 functions as the frequency tuning parameter in this design, resulting in the proposed antenna operating within the confined frequency range of 697.30 to 702.71 MHz. The target 700 MHz operating frequency is achieved when LR7 is set to 6 mm. Fig. 6(a) presents the results for the antenna's width of rectangle7 (WR7) ranges from 69 to 72 mm in 1 mm increments. Simultaneously, the operating frequency varies from 669.00 to 700.00 MHz with exceptional impedance matching ($S_{11} < -10$ dB). The trend suggests that as WR7 increases from 69 to 70 mm, the operating frequency rises, yet an increase from 71 to 72 mm leads to a frequency decrease. WR7 serves as the frequency tuning parameter, guiding the proposed antenna to operate within the frequency range of 697.30 to 702.71 MHz. The desired 700 MHz operating frequency aligns with WR7 of 70 mm. Fig. 6(b) exhibits the response for the length of rectangle8 (LR8) spans from 8 mm to 12 mm with 1 mm increments. The operating frequency varies from 660.00 to 700.00 MHz with excellent impedance matching ($S_{11} < -10$). LR8's role as the frequency tuning parameter is evident in the proposed antenna's operation within the frequency range of 697.30 to 702.71 MHz. The optimal 700 MHz operating frequency is attained when LR8 is set to 10 mm. Fig. 6(c) showcase the antenna performance for length of rectangle9 (LR9) ranges from 4 mm to 8 mm in 1 mm increments. The operating frequency varies from 660.00 to 700.00 MHz with excellent impedance matching ($S_{11} < -10$). LR9 assumes the role of the frequency tuning parameter, guiding the proposed antenna's operation within the frequency range of 697.30 to 702.71 MHz. An optimal 700 MHz operating frequency is achieved when LR9 is set to 6 mm.

Realized gain represents a pivotal antenna characteristic, calculated as four times the intensity of radiation in a specific direction, divided by the total incident power at the antenna port(s). Conversely, peak realized gain signifies the maximum value attained among the realized gains across user-defined directions within the far-field infinite sphere. In the context of realized gain, the reference is the time-averaged power of the incoming wave. Notably, if the imaginary component of impedance greatly surpasses the real part, this value can be exceptionally small, potentially even lower than the recognized power. This implies the possibility of a gain exceeding unity. Equation (1) is considered to compute the realized gain in HFSS.

$$RealizedGain = 4\pi \frac{U}{P_{incident}} \quad (1)$$

Where, U is the radiation intensity in watts per steradian in the selected direction. $P_{incident}$ represents the incident power in watts.

The omni-directional antenna realized gain of the antenna parameters of the different length and width shown in Fig. 7. The realized gain of the antenna has low gain is -3.88 dB at 700 MHz and it also has bandwidth is 16.52 MHz. The omni-directional antenna is operating in the frequency range from 650 MHz to 750 MHz. Fig. 7(a), LG is varying from 38 mm to 42 mm, linear step increases 1 mm, by increases LG from 38 mm to 41 mm, the operating frequency, and also bandwidth decrease, but the LG is 42 mm the operating frequency and bandwidth are slightly increased. Fig. 7(b), WR1 is increasing from 54 mm to 58 mm, linear step increases 1 mm, by increases WR1, both the operating frequency and bandwidth also decreases. Fig. 7(c), WR2 varies from 10 mm to 14 mm, linear step increases 1 mm, by increases WR2, both the operating frequency and bandwidth increases. The omni-directional antenna LG, WR1, WR2, resonant frequency (RF) realized gain (RG), Lower Side Band (LSB), Upper Side Band (USB) and bandwidth (BW) as shown in Table 2.

In Fig. 8, the surface current distribution of the proposed antenna is showcased. Notably, the peak surface current forms an approximate S-shape across the patch, while a smaller portion of surface current is distributed symmetrically across the arms. A comparison of these symmetrical arms reveals lower current flow on the left side as opposed to the right side. The current is also concentrated in the right-hand side stub. This current distribution trend holds for the S-shape patch, symmetrical arm, and right-hand side stub resonators at both 700 MHz and within the frequency band of 697.30-702.71 MHz. Fig. 9 presents the far-field radiation pattern in the E & H plane co-polarization for the omnidirectional antenna. Notably, maximum radiation is observed in the z-direction at θ angles of 0° and 180° , resulting in gains of -3.99 dB and -3.85 dB, respectively. Conversely, the minimum

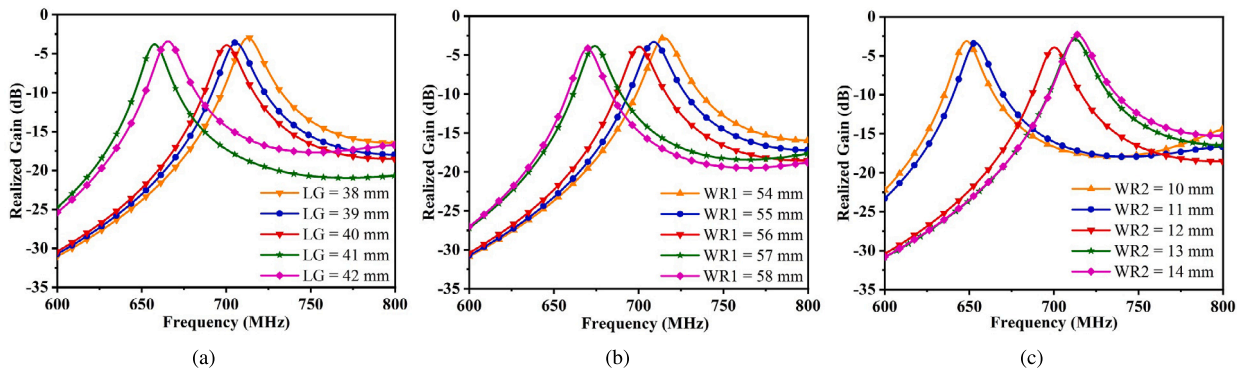


Fig. 7. Parametric analysis of Realized Gain for the proposed antenna (a) LG, (b) WR1, (c) WR2.

Table 2
Realized gain values of the proposed antenna.

Parameter	Value (mm)	MHz				
		RF	RG	LSB	USB	BW
LG	38	712.00	-2.95	704.86	721.89	17.03
	39	705.00	-3.59	697.77	714.49	16.72
	40	700.00	-3.88	692.42	708.94	16.52
	41	657.75	-3.73	650.86	664.85	13.99
	42	664.75	-3.38	658.05	673.77	15.72
WR1	54	715.50	-2.75	706.69	724.45	17.76
	55	708.50	-3.27	700.83	717.98	17.15
	56	700.00	-3.88	692.42	708.94	16.52
	57	673.50	-3.77	666.71	682.33	15.62
	58	670.00	-4.12	662.58	677.60	15.02
WR2	10	649.00	-3.08	641.43	656.10	14.67
	11	654.25	-3.32	646.44	661.73	15.29
	12	700.00	-3.88	692.42	708.94	16.52
	13	712.00	-2.81	704.37	721.57	17.20
	14	713.75	-2.27	705.86	723.17	17.31

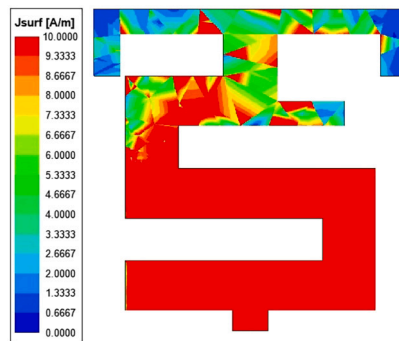


Fig. 8. Surface current density (Jsurf) of the Proposed antenna.

radiation occurs at θ angles of 90° and 270° , yielding gains of -19.12 dB and -19.47 dB, respectively. Fig. 9(a) also depicts the H-plane far-field radiation patterns, showcasing maximum radiation across all angles. Fig. 9(b) displays E-plane far-field radiation patterns in co-polarization and cross-polarization forms. In the E-plane co-polarization patterns, the maximum radiation is observed in the z-direction at θ angles of 0° and 180° , resulting in gains of -4.01 dB and -3.87 dB, respectively. The minimum radiation, on the other hand, occurs at θ angles of 90° and 270° , with gains of -38.57 dB and -37.37 dB, respectively. The cross-polarization pattern for the E-plane shows similar trends. Fig. 9(c) illustrates H-plane far-field radiation patterns in both co-polarization and cross-polarization forms. For the co-polarization pattern, maximum radiation occurs across all angles, while the cross-polarization pattern displays minimum radiation in the z-direction at θ angles of 0° and 180° , with gains of -27.94 dB and -28.21 dB, respectively. The maximum radiation for the cross-polarization pattern occurs at θ angles of 90° and 270° , yielding gains of -19.18 dB and -19.53 dB, respectively. As depicted in Fig. 10, a flexible omnidirectional antenna radiates power equally in all directions perpendicular to

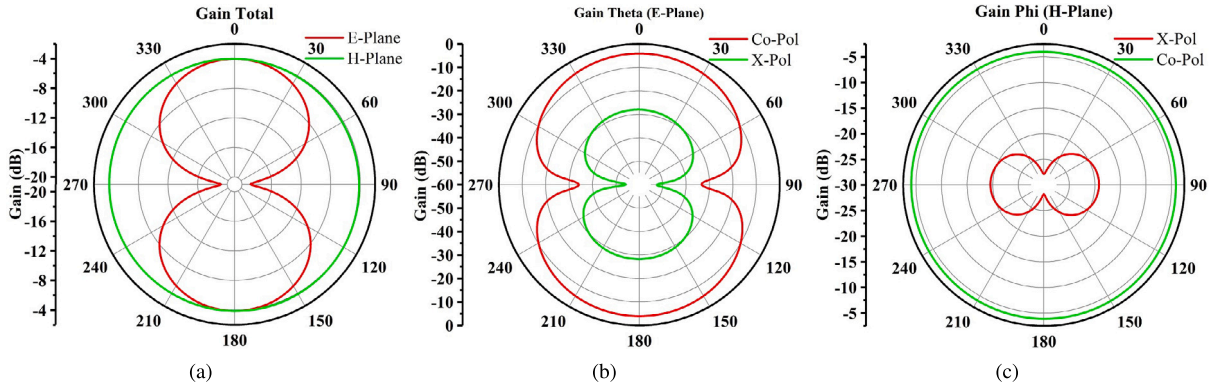


Fig. 9. Omnidirectional antenna radiation pattern at 700 MHz (a) Co-Polarization of E - plane & H - plane (b) E-plane : Co-Polarization for $\phi = 0^\circ$ & Cross Polarization for $\phi = 90^\circ$ (c) H-plane : Cross Polarization for $\phi = 0^\circ$ & Co-Polarization for $\phi = 90^\circ$.

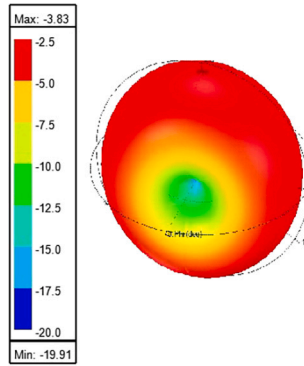


Fig. 10. 3D radiation pattern of the proposed antenna at 700 MHz.

its axis (azimuthal directions). This power strength increases with the angle to the axis (elevation angle) and drops to zero along the axis, forming a characteristic doughnut-shaped radiation pattern in three dimensions. This design contrasts with an isotropic antenna, which radiates uniform power in all directions. Omnidirectional antennas oriented vertically find extensive use in various applications such as radio broadcasting, mobile devices like cell phones and walkie-talkies, wireless networks, cordless phones, GPS systems, and communication base stations like police and taxi dispatchers, as well as aircraft communications. These antennas optimize energy distribution, particularly on the Earth’s surface, minimizing waste and enhancing communication efficiency.

$$a = \frac{F}{\sqrt{1 + \frac{2h}{\pi \epsilon_r F \left[\ln\left(\frac{\pi F}{2h}\right) + 1.776 \right]}}} \tag{2}$$

4. Conformal antenna

In Fig. 11(a), conformal antenna is illustrated, with a patch antenna positioned atop a cylindrical structure. Impedance matching is achieved at a radius of 58° on the cylindrical shape. Fig. 11(b) illustrates the S11 responses of the plain and conformal antennas as per our proposed design. The plain antenna exhibits resonance at 700 MHz, resulting in an S11 of -26.85 dB. In a frequency span ranging from 697.26 to 702.74 MHz, the reflection coefficient consistently remains below -10 dB, providing an impedance bandwidth of 5.48 MHz. The conformal antenna, integrated with a 50Ω microstrip feed, demonstrates good impedance matching with an S11 of -15.02 dB. Resonance is achieved at 703 MHz, and the S11 remains below -10 dB within the frequency range of 700.57 to 704.74 MHz, yielding an impedance bandwidth of 4.17 MHz. It’s worth noting that our analysis of the conformal antenna indicates that extensive bending has an impact on both the resonance frequency and impedance matching, although the S11 value remains well below -10 dB, as shown in Fig. 11(b).

The realized gain of the plain and conformal antennas is displayed in Fig. 11(c). The plain antenna, tuned at 700 MHz, achieves a gain of -3.87 dB. This gain remains within -6.87 dB (3 dB down) bandwidth from 692.45 to 708.88 MHz, with an overall bandwidth of 16.43 MHz. For the conformal antenna, tuned at 703 MHz, the realized gain is -5.54 dB. Within a -8.54 dB (3 dB down) bandwidth from 695.80 to 710.51 MHz, the overall bandwidth is 14.71 MHz. Fig. 7 presents the realized gain of the omni-directional antenna for various lengths and widths. At 700 MHz, the antenna’s realized gain is -3.88 dB, with a bandwidth of 16.52 MHz. It operates within the frequency range of 650 MHz to 750 MHz. In Fig. 7(a), varying LG from 38 mm to 42 mm leads to changes in operating frequency

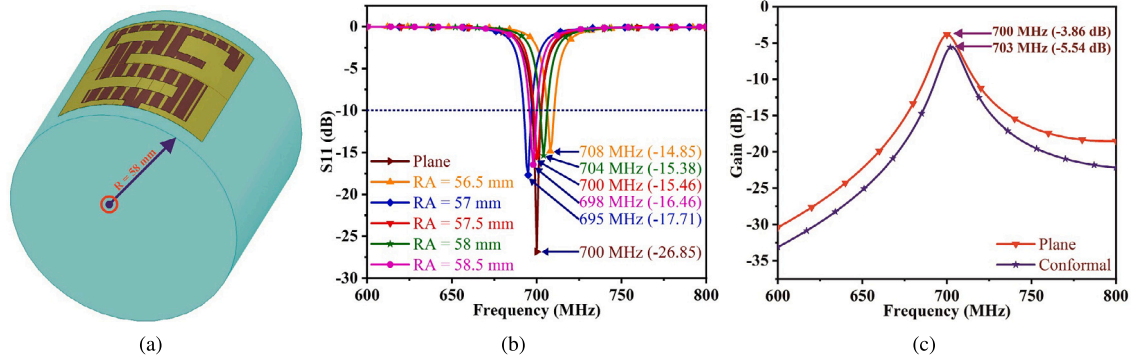


Fig. 11. Conformal analysis (a) Conformal Antenna (b) S11: Plane and Conformal (c) Gain: Plane and Conformal.

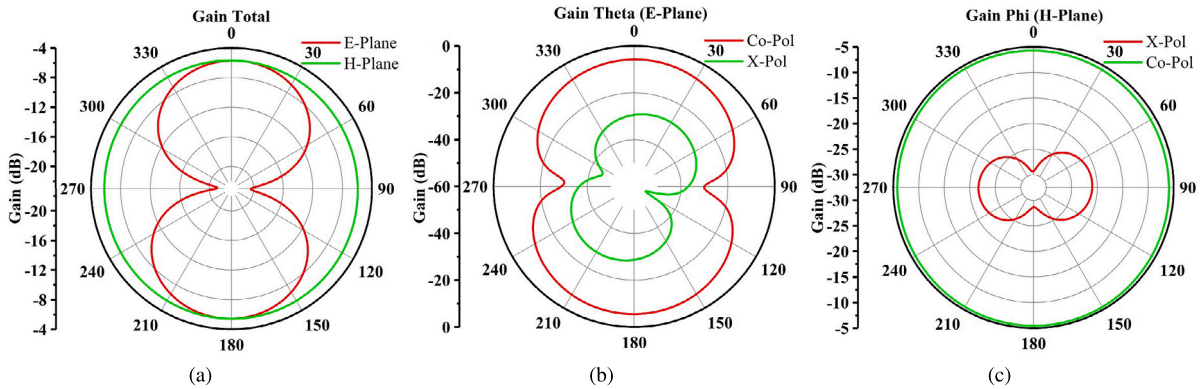


Fig. 12. Conformal antenna radiation pattern at 703 MHz (a) Co-Polarization of E - plane & H - plane (b) E-plane : Co-Polarization for $\phi = 0^\circ$ & Cross Polarization for $\phi = 90^\circ$ (c) H-plane : Cross Polarization for $\phi = 0^\circ$ & Co-Polarization for $\phi = 90^\circ$.

and bandwidth, with a dip when LG reaches 42 mm. Similarly, Fig. 7(b) demonstrates how increasing WR1 from 54 mm to 58 mm reduces both operating frequency and bandwidth. Conversely, Fig. 7(c) illustrates how WR2's increase from 10 mm to 14 mm leads to elevated operating frequency and bandwidth. Fig. 12 displays the radiation pattern of the conformal antenna. Figs. 12(a), 12(b), and 12(c) represents the total gain, E-plane, and H-plane pattern, respectively. In the co-polarization E-plane, maximum radiation occurs in the z-direction at θ angles of 0° and 180° , yielding gains of -5.67 dB and -5.40 dB, while minimum radiation is observed at θ angles of 90° and 270° , resulting in gains of -20.62 dB and -21.25 dB. The H-plane co-polarization pattern shows maximum radiation across all angles. In the E-plane co-polarization pattern, maximum radiation occurs in the z-direction at θ angles of 0° and 180° , yielding gains of -5.69 dB and -5.42 dB, and the minimum radiation is observed at θ angles of 90° and 275° , resulting in gains of -31.93 dB and -30.99 dB. In the cross-polarization form, the E-plane's maximum radiation occurs at θ angles of 30° and 210° , while the minimum radiation is observed at θ angles of 115° and 290° . The H-plane radiation patterns are similar, with maximum radiation at θ angles of 90° and 270° .

4.1. The performance of a wearable antenna near the human body is crucial to assess its Specific Absorption Rate (SAR). SAR measures how electromagnetic power is absorbed by the human body. The Federal Communication Commission (FCC) has set limits on the radiation absorbed by the body and the heating of tissue, following IEEE C95.1-2005, which should not exceed 1.6 W/kg over a 1-gram tissue [24]. As the wearable antennas are mounted above the air-skin interface a tradeoff can be established between the gap of the antenna and the SAR. However, it completely depends on the application. In this study, a cylindrical human hand phantom is modeled as shown in Fig. 13(a). The phantom includes the bone, muscle, fat and skin. The antenna is placed above 5 mm to the phantom and the SAR on the phantom is evaluated. The SAR for the proposed human hand model is found satisfactory, as shown in Fig. 13(b). The proposed antenna can be used for a commercial application where a minimum air-gap of 5 mm between antenna and the skin is required.

5. Fabrication and testing

To test the scattering parameters, the vector-network-analyzer undergoes calibration through utilization of a mechanical calibration kit, wherein the center frequencies are set at 500 MHz and 900 MHz. Subsequently, with the vector network analyzer properly configured, various impedance matching parameters are obtained. In an open environment, the antenna's radiation pattern is evaluated employing an RF source, RF detector, and an automated data logging system. Care is taken to maintain a non-reflective

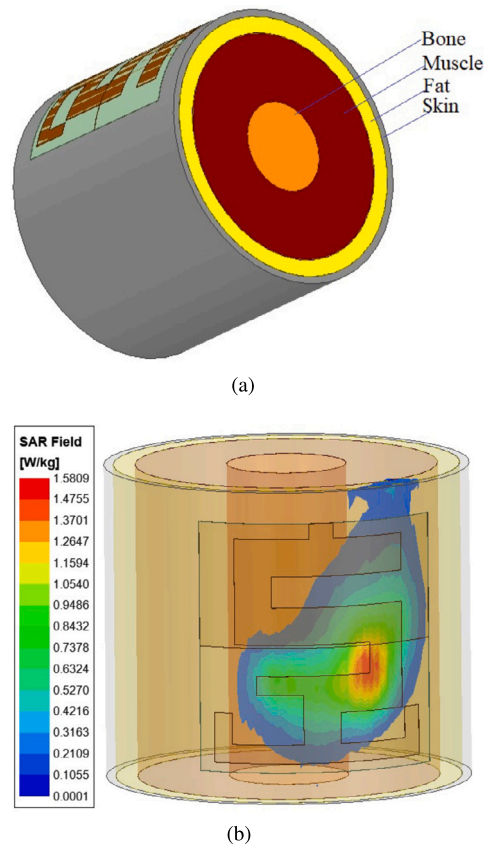


Fig. 13. Setup and result of SAR analysis (a) Setup (b) Simulated SAR.

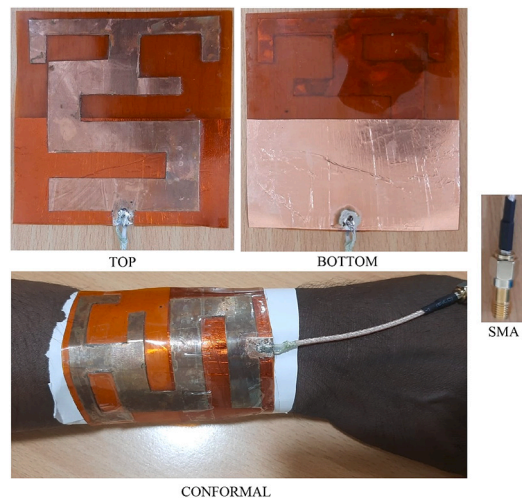


Fig. 14. Prototype of the Flexible omni-directional antenna.

environment to guarantee the precision of the measurements. The antenna’s prototype has been developed, as depicted in Fig. 14. This prototype involves an antenna fabricated on an ultra-thin 0.25 mm polyimide substrate, coated with a Copper foil layer. To assess the antenna’s performance, a coaxial cable is linked to a 50 Ω Jack sub-miniature version-A (SMA) connector with an operating frequency range of 18 GHz. This cable is connected to the coplanar microstrip feed. The antenna’s prototype, along with a comparative analysis of simulated and measured parameters, is presented in Fig. 15. The proposed antenna demonstrates a good agreement between the simulated and measured scattering parameters. Across a fractional bandwidth of 18.57%, spanning from 25.4 to 30.6 GHz, the antenna’s effectiveness is depicted in Fig. 15(a). In addition, the measured scattering parameter in conformal state

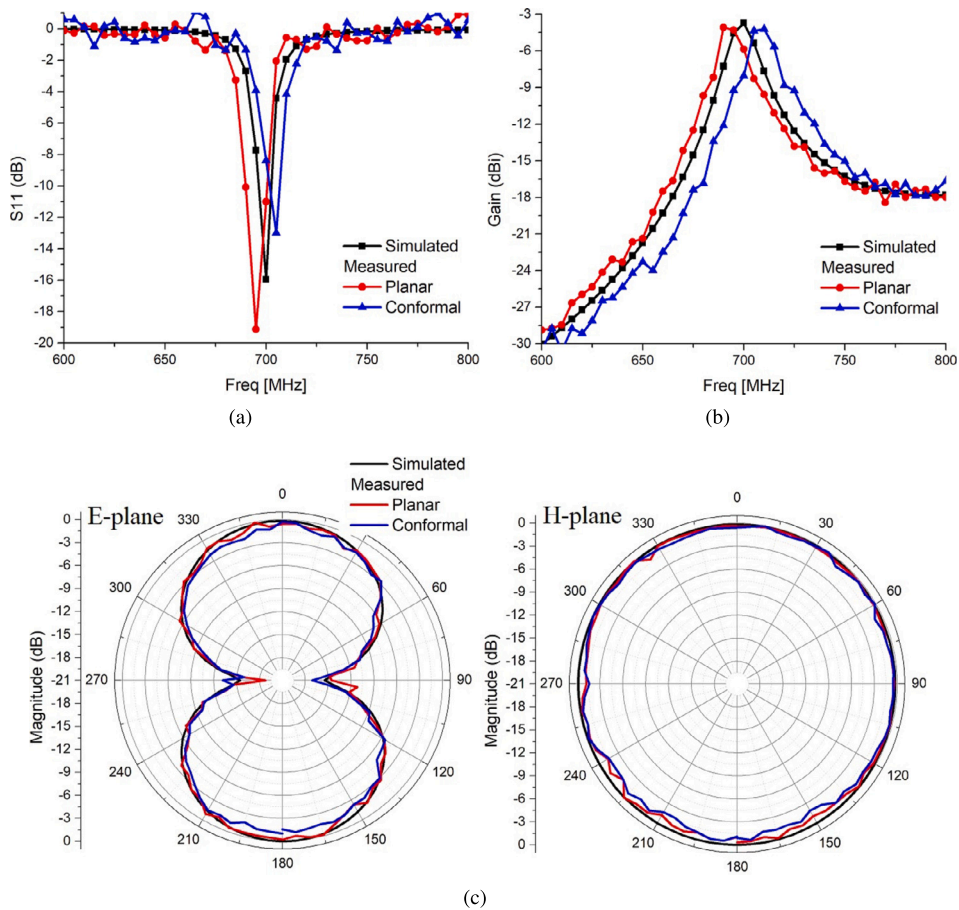


Fig. 15. Simulated and measured results in planar and conformal modes (a) S_{11} (b) Gain (c) E and H-plane radiation at 700 MHzZ.

is also satisfactory, as shown in Fig. 15(a). For the measurement of realized gain, a dual antenna technique is employed. Initially, two well-defined antennas within the same frequency bands function as both transmitters and receivers in a two-port vector network analyzer setup. The S_{21} parameter is recorded. Subsequently, one of these reference antennas is substituted with the antenna under test (AUT), and the S_{21} parameter is once again measured. The dissimilarities between the reference antenna and the AUT's performance establish the realized gain of the proposed antenna. The measured gain is slightly lower than the simulated gain due to inherent fabrication and measurement inaccuracies. Nevertheless, the antenna's gain remains satisfactory for low-frequency operations across the entire spectrum, as shown in Fig. 15(b). The proposed antenna exhibits an omnidirectional radiation pattern, an attribute affirmed by the measured radiation pattern shown in Fig. 15(c). The complete E-plane radiation is extracted by considering a theta range of -180 to $+180$ degrees and a phi value of 0 degrees. Further validation is provided by the measured E-plane co-polarization and cross-polarization radiation patterns, depicted in Fig. 15(c). This visualization confirms the antenna's omnidirectional radiation characteristics, underscored by a substantial level of co and cross-polarization isolation, rendering it suitable for communication systems.

Table 3 highlights the superiority of the proposed antenna. To gauge its performance, we have evaluated it against some antennas reported in the literature. These antennas have been specifically designed for conformal and, in many cases, body-centric applications. Our proposed antenna stands out due to its lower-profile design and its ability to radiate in an omnidirectional pattern. The antenna presented in [19] achieves a low profile as well, although it radiates in a directional radiation pattern. In addition, the proposed antenna achieves 40% miniaturization compared to a conventional rectangular patch antenna.

6. Conclusion

An innovative compact conformal antenna with a meander-line design is introduced for the CWSCA 700 MHz band. This novel configuration has been meticulously adjusted to ensure optimal functionality within both the planar and conformal modes, specifically tailored for the 700 MHz frequency range. The conformal characteristics of the design were evaluated by wrapping it around a human wrist, and subsequent performance measurements were taken. Although the antenna's small size and limited effective aperture lead to a relatively modest gain, this is deemed satisfactory for its intended use in low-frequency operations. Notably, the

Table 3
Comparison table.

Ref.	Frequency band (GHz)	Technique (s)	Size ($\lambda \times \lambda$), Free space	Application	Substrate	Conformal	Radiation pattern
[5]	2.45/5.8	Meander line/partial ground	0.048	Body centric	Polyimide	Yes	Quasi-omnidirectional
[7]	2.4	Conventional rectangular patch	NA	Body centric	Ceramic-Doped Silicone	Yes	Quasi-omnidirectional
[9]	1.8	Meander line inspired	0.077	Body centric	Rogers Duriod 5880	Yes	Omnidirectional
[15]	3.4	Metamaterial	0.336	Body centric	Rogers Duriod 5880	Yes	Omnidirectional
[19]	0.9	Inverted-F	0.004	Body centric	Rogers RO3010	Yes	Directional
[21]	3.89-5.9	Co-planar annular ring	0.307	WLAN	Polyethylene terephthalate	Yes	Directional
[22]	2.21-6	Co-planar annular ring/partial ground	0.158	WLAN	Melinex	Yes	Omnidirectional
Proposed work	0.7	Meander line/ partial ground	0.0348	Body centric	Polyimide	Yes	Omnidirectional

antenna exhibits an ideal omnidirectional radiation pattern, a crucial attribute for CWSCA applications. The alignment between the results obtained from simulations and actual measurements validates the successful execution of the proposed design.

CRedit authorship contribution statement

Ravi Kumar Thella: Validation, Software, Investigation, Formal analysis. **Jayendra Kumar:** Writing – review & editing, Supervision, Methodology, Conceptualization.

Declaration of competing interest

The authors declare that they have no known competing financial interests or personal relationships that could have appeared to influence the work reported in this paper.

References

- [1] R. Xu, Z. Shen, Wideband ferrite-loaded bow-tie antenna of extremely low-profile, *IEEE Trans. Antennas Propag.* 70 (12) (Dec. 2022) 11401–11409, <https://doi.org/10.1109/TAP.2022.3209706>.
- [2] T. Pei, L. Zhu, J. Wang, W. Wu, A low-profile decoupling structure for mutual coupling suppression in MIMO patch antenna, *IEEE Trans. Antennas Propag.* 69 (10) (Oct. 2021) 6145–6153, <https://doi.org/10.1109/TAP.2021.3098565>.
- [3] S.-J. Wu, C.-H. Kang, K.-H. Chen, J.-H. Tarng, A multiband quasi-Yagi type antenna, *IEEE Trans. Antennas Propag.* 58 (2) (Feb. 2010) 593–596, <https://doi.org/10.1109/TAP.2010.2041522>.
- [4] S.-T. Wang, L. Zhu, H. Deng, Design approach for pattern-reconfigurable patch antenna without extra feeding networks, *IEEE Trans. Antennas Propag.* 71 (2) (Feb. 2023) 1925–1930, <https://doi.org/10.1109/TAP.2022.3229179>.
- [5] M. Wang, et al., Investigation of SAR reduction using flexible antenna with metamaterial structure in wireless body area network, *IEEE Trans. Antennas Propag.* 66 (6) (June 2018) 3076–3086, <https://doi.org/10.1109/TAP.2018.2820733>.
- [6] O.M. Sanusi, F.A. Ghaffar, A. Shamim, M. Vaseem, Y. Wang, L. Roy, Development of a 2.45 GHz antenna for flexible compact radiation dosimeter tags, *IEEE Trans. Antennas Propag.* 67 (8) (Aug. 2019) 5063–5072, <https://doi.org/10.1109/TAP.2019.2911647>.
- [7] L. Catarinucci, F.P. Chietera, R. Colella, Permittivity-customizable ceramic-doped silicone substrates shaped with 3-D-printed molds to design flexible and conformal antennas, *IEEE Trans. Antennas Propag.* 68 (6) (June 2020) 4967–4972, <https://doi.org/10.1109/TAP.2020.2969748>.
- [8] Z.-X. Liu, L. Zhu, N.-W. Liu, Design approach for compact dual-band dual-mode patch antenna with flexible frequency ratio, *IEEE Trans. Antennas Propag.* 68 (8) (Aug. 2020) 6401–6406, <https://doi.org/10.1109/TAP.2020.2992809>.
- [9] X. Chen, M.-C. Tang, D. Li, M. Li, Flexible, bandwidth-enhanced, electrically small, electric near-field resonant parasitic antenna with filtering performance characteristics, *IEEE Trans. Antennas Propag.* 70 (6) (June 2022) 4860–4865, <https://doi.org/10.1109/TAP.2021.3137502>.
- [10] C.H. Wang, X.M. Shi, H.L. Yang, X.L. Xi, A flexible amplitude equalizing filter based on spoof surface plasmon polaritons, *IEEE Trans. Antennas Propag.* 71 (7) (July 2023) 5777–5785, <https://doi.org/10.1109/TAP.2023.3266864>.
- [11] P. Liu, Z. Meng, L. Wang, Y. Zhang, Y. Li, Omnidirectional dual-polarized saber antenna with low wind drag, *IEEE Trans. Antennas Propag.* 68 (1) (Jan. 2020) 558–563, <https://doi.org/10.1109/TAP.2019.2934566>.
- [12] Y. He, Y. Li, L. Zhu, P.-Y. Chen, Miniaturization of omnidirectional cavity antennas using substrate-integrated impedance surfaces, *IEEE Trans. Antennas Propag.* 69 (3) (March 2021) 1728–1733, <https://doi.org/10.1109/TAP.2020.3012493>.
- [13] Y. Zhang, Y. Li, Scalable omnidirectional dual-polarized antenna using cavity and slot-dipole hybrid structure, *IEEE Trans. Antennas Propag.* 70 (6) (June 2022) 4215–4223, <https://doi.org/10.1109/TAP.2021.3138552>.
- [14] S.-Y. Ooi, P.-S. Chee, E.-H. Lim, J.-H. Low, F.-L. Bong, A zeroth-order slot-loaded cap-shaped patch antenna with omnidirectional radiation characteristic for UHF RFID tag design, *IEEE Trans. Antennas Propag.* 71 (1) (Jan. 2023) 131–139, <https://doi.org/10.1109/TAP.2022.3221032>.
- [15] Bidisha Hazarika, Banani Basu, Jayendra Kumar, A multi-layered dual-band on-body conformal integrated antenna for WBAN communication, *AEÜ, Int. J. Electron. Commun.* 95 (2018) 226–235, <https://doi.org/10.1016/j.aeue.2018.08.021>.
- [16] Y.F. Wu, Y.J. Cheng, Proactive conformal antenna array for near-field beam focusing and steering based on curved substrate integrated waveguide, *IEEE Trans. Antennas Propag.* 67 (4) (April 2019) 2354–2363, <https://doi.org/10.1109/TAP.2019.2891725>.
- [17] X. Tian, Q. Zeng, D. Nikolayev, J.S. Ho, Conformal propagation and near-omnidirectional radiation with surface plasmonic clothing, *IEEE Trans. Antennas Propag.* 68 (11) (Nov. 2020) 7309–7319, <https://doi.org/10.1109/TAP.2020.2998216>.

- [18] Y. Gao, W. Jiang, W. Hu, Q. Wang, W. Zhang, S. Gong, A dual-polarized 2-D monopulse antenna array for conical conformal applications, *IEEE Trans. Antennas Propag.* 69 (9) (Sept. 2021) 5479–5488, <https://doi.org/10.1109/TAP.2021.3060085>.
- [19] Y. Wang, S. Yan, B. Huang, Conformal folded inverted-F antenna with quasi-isotropic radiation pattern for robust communication in capsule endoscopy applications, *IEEE Trans. Antennas Propag.* 70 (8) (Aug. 2022) 6537–6550, <https://doi.org/10.1109/TAP.2022.3161342>.
- [20] M.A.C. Zadeh, N. Komjani, Flat-topped radiation pattern synthesis of a conformal leaky-wave holographic antenna, *IEEE Trans. Antennas Propag.* 71 (5) (May 2023) 4045–4054, <https://doi.org/10.1109/TAP.2023.3255556>.
- [21] J.J. Adams, S.C. Slimmer, T.F. Malkowski, E.B. Duoss, J.A. Lewis, J.T. Bernhard, Comparison of spherical antennas fabricated via conformal printing: helix, meanderline, and hybrid designs, *IEEE Antennas Wirel. Propag. Lett.* 10 (2011) 1425–1428, <https://doi.org/10.1109/LAWP.2011.2178999>.
- [22] A. Zhao, J. Zhang, G.Y. Tian, Miniaturization of UHF RFID tag antenna sensors for corrosion characterization, *IEEE Sens. J.* 17 (23) (Dec. 1, 2017) 7908–7916, <https://doi.org/10.1109/JSEN.2017.2751587>.
- [23] D.V.S. Prasad, H.V. Singh, S. Tripathi, P.P. Paltani, In-band full-duplex co-radiator antenna with high isolation using differential-feed and dual-polarization for 2.4 GHz WLAN, *IEEE Antennas Wirel. Propag. Lett.* 22 (11) (2023) 2740–2744, <https://doi.org/10.1109/LAWP.2023.3297599>.
- [24] J. Kumar, B. Basu, F.A. Talukdar, Modeling of a PIN diode RF switch for reconfigurable antenna application, *Sci. Iran.* 26 (3) (2019) 1714–1723, <https://doi.org/10.24200/sci.2018.20110>.